

## X-RAY ABSORPTION ANALYSIS OF NGC 3516: APPEARANCE OF FAST COMPONENTS WITH INCREASED SOURCE FLUX

TOMER HOLCZER AND EHUD BEHAR

Department of Physics, Technion, Haifa 32000, Israel; tomer@physics.technion.ac.il, behar@physics.technion.ac.il  
Received 2011 September 21; accepted 2011 December 13; published 2012 February 15

### ABSTRACT

By analyzing the X-ray spectra of NGC 3516 from 2001 and 2006 obtained with the HETGS spectrometer on board the *Chandra* X-ray Observatory, we find that the kinematic structure of the outflow can be well represented by four outflow components intrinsic to NGC 3516:  $-350 \pm 100 \text{ km s}^{-1}$ ,  $-1500 \pm 150 \text{ km s}^{-1}$ ,  $-2600 \pm 200 \text{ km s}^{-1}$ , and  $-4000 \pm 400 \text{ km s}^{-1}$ . A local component at  $z = 0$  could be confused in the spectrum with intrinsic component 3. Components 1 and 2 have a broad range of ionization manifested by absorption from 23 different charge states of Fe. Components 3 and 4 are more highly ionized and show absorption from only nine different charge states of Fe. However, we were able to reconstruct the absorption measure distribution for all four. The total column density of each component is  $N_{\text{H}} = (1.8 \pm 0.5) \times 10^{22} \text{ cm}^{-2}$ ,  $(2.5 \pm 0.3) \times 10^{22} \text{ cm}^{-2}$ ,  $(6.9 \pm 4.3) \times 10^{22} \text{ cm}^{-2}$ , and  $(5.4 \pm 1.2) \times 10^{22} \text{ cm}^{-2}$ , respectively. The fast components 3 and 4 appear only in the high state of 2006 and not in 2001, while the slower components persist during both epochs. On the other hand, there is no significant absorption variability within days during 2001 or 2006. We find that the covering factor plays a minor role for the line absorption.

*Key words:* galaxies: active – galaxies: individual (NGC 3516) – galaxies: Seyfert – line: formation

*Online-only material:* color figures

### 1. INTRODUCTION

Approximately half of type 1 active galactic nuclei (AGNs) show complex absorption in the soft X-ray band (Crenshaw et al. 2003; Piconcelli et al. 2005). The blueshifted absorption lines come from a highly or partly ionized outflow first noted by Halpern (1984). These outflows may play a central role in cosmological feedback, in the metal enrichment of the intergalactic medium, and in understanding black hole evolution. However, the outflow physical properties such as mass, energy, and momentum are still largely unknown. A necessary step to advance on these issues is to obtain reliable measurements of the ionization distribution and column densities of the outflowing material as well as the location of these outflows in order to determine the mass outflow.

NGC 3516 is a Seyfert 1 galaxy at a redshift  $z = 0.008836$  (Keel 1996). It exhibits a variable relativistic Fe  $K\alpha$  emission line (Nandra et al. 1997, 1999) which could consist of a few narrow components (Turner et al. 2002). UV observations of NGC 3516 showed several outflowing components. Kriss et al. (1996a) found a low velocity component of  $\sim -300 \text{ km s}^{-1}$  while also observing lines at close to the systemic redshift velocity ( $-2649 \text{ km s}^{-1}$ ). Crenshaw et al. (1999) revealed four slow components with outflowing velocities of  $-31$ ,  $-88$ ,  $-148$ , and  $-372 \text{ km s}^{-1}$ . Kraemer et al. (2002) later detected UV absorption up to velocities of  $-1300 \text{ km s}^{-1}$ .

There are many studies in the literature of the ionized X-ray absorber of NGC 3516, the most important of which are listed in Table 1. Not all reports on the outflow of NGC 3516 are consistent, as described below. Kolman et al. (1993) analyzed a *Ginga* observation from 1989 and found an absorber with a partial covering factor. Mathur et al. (1997) found a  $-500 \text{ km s}^{-1}$  outflowing component using a *ROSAT* observation from 1992. Kriss et al. (1996b) fitted *ASCA* data from 1994 with two absorption components, both outflowing with  $< -120 \text{ km s}^{-1}$ . Reynolds (1997) fitted the 1995 *ASCA* data with a single component. Costantini et al. (2000) studied *BeppoSAX* data

from 1996 and 1997 and fitted two ionization components outflowing at velocities of  $-500 \text{ km s}^{-1}$ . Netzer et al. (2002) fitted *ASCA* data from 1998 and *Chandra* LETG data from 2000 with a single component. Using 2001 partially simultaneous *Chandra*, *BeppoSAX*, and *XMM-Newton* observations, Turner et al. (2005) identified three components: the  $-200 \text{ km s}^{-1}$  component was called the “UV absorber,” the second was called “High” at  $-1100 \text{ km s}^{-1}$ , and the third that was called “Heavy” was also at  $-1100 \text{ km s}^{-1}$ , but coverage of the source varied, which explained changes in the continuum curvature. Markowitz et al. (2008), based on a *Suzaku* 2005 observation, found two components: one was fitted with an outflow velocity of  $-1100 \text{ km s}^{-1}$ , while the other was stationary. Turner et al. (2008) studied *Chandra* and *XMM-Newton* observations from 2006 and identified four components. Two components were static while the third (“heavy” which also had a partial covering factor) and fourth (“high”) had higher outflow velocities of  $-1575$  and  $-1000 \text{ km s}^{-1}$ , respectively. Recently, Mehdipour et al. (2010) analyzed an *XMM-Newton* observation of NGC 3516 from 2006 and identified three components outflowing at velocities of  $-100$ ,  $-900$ , and  $-1500 \text{ km s}^{-1}$ . The fastest component also had a partial covering factor.

In this paper, we wish to provide a definitive investigation of the physical conditions in the NGC 3516 X-ray absorber, using the archival HETGS observation from 2001 and 2006 and exploiting its high spectral resolution, but with special focus on the ionization distribution of the plasma and on lines that do not seem to fit the simple two-velocity picture. While the majority of studies on the X-ray spectra of AGN outflows employ gradually increasing numbers of ionization components until the fit is satisfactory (e.g., Kaspi et al. 2001; Sako et al. 2003), it is instructive to reconstruct the actual distribution of the column density in the plasma as a continuous function of ionization parameter  $\xi$  (Steenbrugge et al. 2005), which we termed the absorption measure distribution (AMD; Holczer et al. 2007). Although for high-quality spectra such as the present one, two or three ionization components might produce a satisfactory fit,

**Table 1**  
Historical Observations of NGC 3516

Observatory	Year	Duration (ks)	Flux Level at 1 keV ( $10^{-3}$ photon $\text{cm}^{-2}$ $\text{s}^{-1}$ $\text{keV}^{-1}$ )	References <sup>a</sup>
<i>Ginga</i>	1989 Oct	20	$6 \pm 1$	1
<i>ROSAT</i>	1992 Oct	13	$17 \pm 3$	2
<i>ASCA</i>	1994 Apr	28	<sup>b</sup> $13 \pm 2$	3
<i>ASCA</i>	1995 Mar	33	<sup>b</sup> $7 \pm 1$	4
<i>BeppoSAX</i>	1996 Nov	16	$1 \pm 0.5$	5
<i>BeppoSAX</i>	1997 Mar	16	$7 \pm 2$	5
<i>ASCA</i>	1998 Apr	360	<sup>b</sup> $3 \pm 0.5$	6
<i>Chandra</i>	2000 Oct	47	<sup>b</sup> $0.6 \pm 0.2$	6
<i>Chandra</i>	2001 Apr	119	$1.5 \pm 0.2$	7,11
<i>XMM-Newton</i>	2001 Apr	49	$1.7 \pm 0.2$	7
<i>Chandra</i>	2001 Nov	88	$0.9 \pm 0.2$	7,11
<i>XMM-Newton</i>	2001 Nov	49	$1 \pm 0.2$	7
<i>Suzaku</i>	2005 Oct	135	$0.6 \pm 0.2$	8
<i>Chandra</i>	2006 Oct	200	$5 \pm 0.5$	9,11
<i>XMM-Newton</i>	2006 Oct	155	$5 \pm 0.5$	9,10,11

#### Notes.

<sup>a</sup> (1) Kolman et al. 1993; (2) Mathur et al. 1997; (3) Reynolds 1997; (4) Kriss et al. 1996b; (5) Costantini et al. 2000; (6) Netzer et al. 2002; (7) Turner et al. 2005; (8) Markowitz et al. 2008; (9) Turner et al. 2008; (10) Mehdipour et al. 2010; (11) present work.

<sup>b</sup> Netzer et al. (2002) finding of long-term decline over years is fortuitous.

the AMD reconstruction is the only method that reveals the actual distribution including its physical discontinuities (e.g., due to thermal instability), and ultimately provides a more precise measurement of the total column density. Furthermore, the AMD shape can impose tight constraints on physical outflow models and on the density distribution in the outflow (Chelouche 2008; Behar 2009; Fukumura et al. 2010, 2011).

## 2. DATA REDUCTION

NGC 3516 was observed by *Chandra*/HETGS on 2001 April 9–10 and November 11, as well as on 2006 October 9–14 for a total exposure time of 407 ks. In each observation, the first three high energy gratings (HEG) and medium energy gratings (MEG) refraction orders ( $\pm 1, 2, 3$ ) were reduced from the *Chandra* archive using the standard pipeline software (CIAO version 4.1.2). The total number of counts in the first order ( $\pm 1$ ) between 2 and 25 Å is 141,663 for MEG and 75,043 for HEG. More details on the observations can be found in Table 2. No background subtraction was required as the background level was negligible. Flux spectra were obtained by first co-adding count spectra and convoluting with the broadest line-spread function (MEG first order) to

ensure uniformity. The total count spectra were then divided by the total effective area curve (summed over orders) and observation time. Finally, spectra were corrected for neutral Galactic absorption of  $N_{\text{H}} = 3.23 \times 10^{20} \text{ cm}^{-2}$  (Dickey & Lockman 1990). Spectra from 2001 April, 2001 November, and 2006 October are presented in Figure 1 with a binning of 50 mÅ.

## 3. SPECTRAL MODEL

Variations of approximately 40% on timescales of a few ks were observed during both the 2001 and 2006 observations of NGC 3516. The average X-ray flux of NGC 3516 varies greatly over the span of the 17 years it has been observed, as can be seen from the continuum flux levels quoted in Table 1. The difference between minimum and maximum reaches a factor of  $\sim 10$ –30 on timescales of a few months, in contrast to the impression given by the sequence of observations reported in Netzer et al. (2002) of slow decay in flux over a few years. The present work deals with the mean properties of the ionized absorber. As a first step we reduce a spectrum from each separate observation. It can be seen from Figure 1 that on a timescale of a day, the average flux varies by a factor of a few, during both the 2001 observations (from black to red) and the 2006 observations (from cyan to yellow).

Since the 2001 flux is consistently lower than that of 2006, we combine the three observations from 2001 (low state) separately from the five 2006 observations (high state). Combining the spectra was carried out by first adding all of the counts and only then dividing them by the time-weighted sum of the effective area and total exposure time. The flux level in the 2006 observation was on average five times higher than in 2001. The high- and low-state spectra are shown in Figure 2 with a binning of 50 mÅ.

It can be seen that the 2006 spectrum shows much better resolved absorption troughs and was used in order to obtain the warm absorber parameters. The fitting procedure follows our ion-by-ion fitting method (Behar et al. 2001a, 2003; Sako et al. 2001; Holczer et al. 2005). First, we fit for the broadband continuum. Subsequently, we fit the absorption features using template ionic spectra that include all of the absorption lines and photoelectric edges of each ion, but vary with the broadening (so-called turbulent) velocity and the ionic column density. A covering factor of unity is used throughout this process. The “black” troughs of the leading lines of  $\text{O}^{+6}$  and  $\text{O}^{+7}$  strongly support this assumption. Strong emission lines are fitted as well. The emission lines are added after the absorption components were modeled (hence, the emission lines are not absorbed). Another interesting feature that can be seen in Figure 2 is the softening of the spectrum at higher flux levels. This was already

**Table 2**  
*Chandra* Observations of NGC 3516 Used in This Work

ObsID	Start Date	Detector	Gratings	Exposure (s)	Counts in HEG orders $\pm 1$	Counts in MEG orders $\pm 1$
2431	2001 Apr 9	ACIS-S	HETG	35568	2383	4143
2080	2001 Apr 10	ACIS-S	HETG	73332	9019	16057
2482	2001 Nov 11	ACIS-S	HETG	88002	6393	11181
8452	2006 Oct 9	ACIS-S	HETG	19831	6245	12024
7282	2006 Oct 10	ACIS-S	HETG	41410	9176	16906
8451	2006 Oct 11	ACIS-S	HETG	47360	17482	34473
8450	2006 Oct 12	ACIS-S	HETG	38505	14773	29920
7281	2006 Oct 14	ACIS-S	HETG	42443	9572	16959

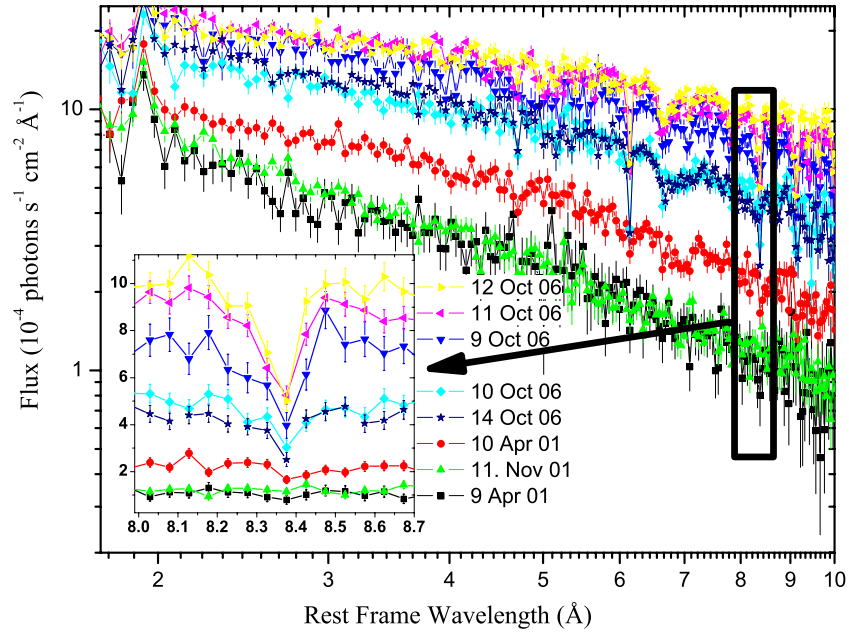


**Figure 1.** *Chandra* HETGS spectra of NGC 3516 corrected for cosmological redshift ( $z = 0.008836$ ) and binned to  $50 \text{ m}\text{\AA}$ . Observation dates are listed in the legend. No absorption variability is observed on timescales of days.

(A color version of this figure is available in the online journal.)

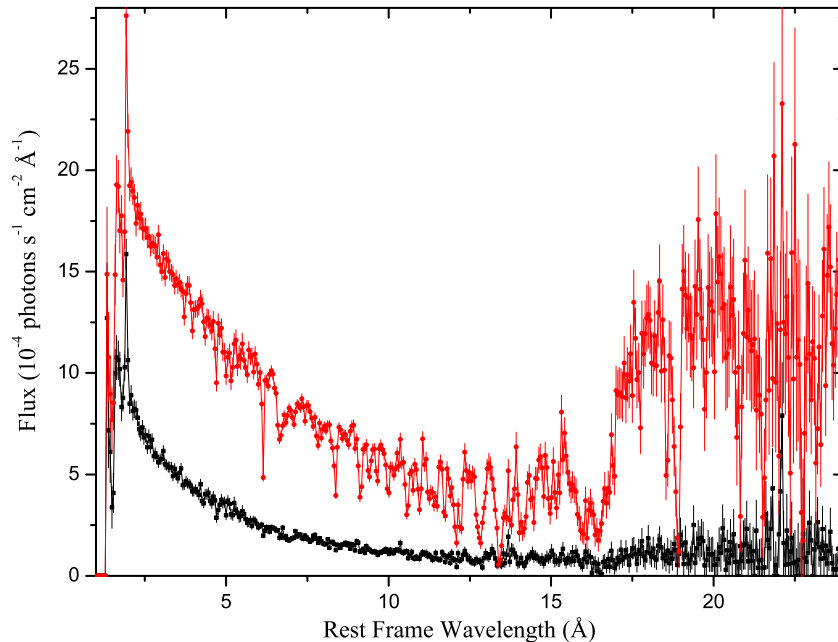


**Figure 2.** *Chandra* HETGS spectrum of NGC 3516 corrected for cosmological redshift ( $z = 0.008836$ ) and binned to  $50 \text{ m}\text{\AA}$ . The red and black lines represent the average flux from the 2006 and 2001 observations, respectively.

(A color version of this figure is available in the online journal.)

observed for NGC 3783 (Netzer et al. 2003) and in fact expected from the cooling of a comptonizing corona above the accretion disk (Haardt et al. 2001).

### 3.1. Continuum Parameters

The continuum X-ray spectrum of most AGNs can be characterized by a high-energy power law and a soft excess that rises above the power law below  $\sim 1 \text{ keV}$ . This soft excess is often modeled with a blackbody, or modified blackbody, although it is clearly more spectrally complex and possibly includes atomic features. For the 2006 spectra, we used a power law with a pho-

ton spectral index of  $\Gamma = 1.48$ , which was fitted to the  $2\text{--}6 \text{ \AA}$  band, and a blackbody temperature of  $kT = 110 \text{ eV}$ . This is a rather flat slope, which could be due to the band in which it is fitted, but it still provides a good fit to the spectrum (see Figure 4).

### 3.2. The Ionized Absorber

The intensity spectrum  $I_{ij}(\nu)$  around an atomic absorption line  $i \rightarrow j$  can be expressed as

$$I_{ij}(\nu) = I_0(\nu)e^{-N_{\text{ion}}\sigma_{ij}(\nu)}, \quad (1)$$

where  $I_0(\nu)$  represents the unabsorbed continuum intensity and  $\sigma_{ij}(\nu)$  denotes the line absorption cross section for photoexcitation (in  $\text{cm}^2$ ) from ground level  $i$  to excited level  $j$ . If all ions are essentially in the ground level,  $N_{\text{ion}}$  is the total ionic column density toward the source (in  $\text{cm}^{-2}$ ). The photoexcitation cross section is given by

$$\sigma_{ij}(\nu) = \frac{\pi e^2}{m_e c} f_{ij} \phi(\nu), \quad (2)$$

where the first term is a constant that includes the electron charge  $e$ , its mass  $m_e$ , and the speed of light  $c$ . The absorption oscillator strength is denoted by  $f_{ij}$ , and  $\phi(\nu)$  represents the Voigt profile due to the convolution of natural (Lorentzian) and Doppler (Gaussian) line broadening. The Doppler broadening consists of thermal and turbulent motion, but in AGN outflows the turbulent broadening is believed to dominate the temperature broadening. The natural broadening becomes important when the lines saturate as in our current spectrum, e.g., the  $\text{O}^{+6}$  line. Transition wavelengths, natural widths, and oscillator strengths were calculated using the Hebrew University Lawrence Livermore Atomic Code (Bar-Shalom et al. 2001). Particularly important for AGN outflows are the inner-shell absorption lines (Behar et al. 2001b; Behar & Netzer 2002). More recent and improved atomic data for the Fe M-shell ions were incorporated from Gu et al. (2006). These atomic wavelengths were tested against the HETG spectra of NGC 3783 (Behar & Netzer 2002; Netzer et al. 2003; Gu et al. 2006; Holczer et al. 2007) and found to agree with the data to within the instrumental precision.

Since the absorbing gas is outflowing, the absorption lines are slightly blueshifted with respect to the AGN rest frame. Although blueshifts of individual lines can differ to a small degree, we can identify two kinematic components with best-fit outflow velocities of  $v = -350 \pm 100 \text{ km s}^{-1}$  and  $v = -1500 \pm 150 \text{ km s}^{-1}$  which we call component 1 and component 2, respectively. We also identify two high ionization components at  $v = -2600 \pm 200 \text{ km s}^{-1}$  and  $v = -4000 \pm 400 \text{ km s}^{-1}$  (component 3 and component 4, respectively). The velocities are set in the model to one value (for each component) for all of the ions. Figure 3 shows the absorption troughs of Si and Mg K-shell ions as well as  $\text{Fe}^{+16}$ ,  $\text{Fe}^{+19}$ ,  $\text{Fe}^{+21}$ , and  $\text{Fe}^{+23}$  in velocity space, where the vertical blue lines represent the best-fit velocity components. The first two components are detected in all ions while component 3 has more subtle clues, like a “knee” in the troughs of  $\text{Si}^{+12}$ ,  $\text{Si}^{+13}$ , and  $\text{Mg}^{+11}$ , or a shallow trough in  $\text{Mg}^{+10}$  and  $\text{Fe}^{+21}$ , and a much clearer trough in  $\text{Fe}^{+23}$ . Component 4 is even harder to detect. There are signs for it either as a small “knee” or very small troughs. The broad  $\text{K}\alpha$  troughs of  $\text{Fe}^{+24}$  and  $\text{Fe}^{+25}$ , not shown in Figure 3, also extend from  $\sim 0$ – $4000 \text{ km s}^{-1}$ . However, this result cannot be too meaningful, as the instrumental resolution at these lines is worse than  $3000 \text{ km s}^{-1}$ .  $\text{Fe}^{+16}$  does not show absorption from the faster components 3 and 4, and we conclude these two components appear only in higher ionization states. Above  $\sim 20 \text{ \AA}$  there are absorption lines mostly from oxygen which appear to have a high velocity component matching the third component ( $-2600 \text{ km s}^{-1}$ ), but could also be local ( $z = 0$ ), which is discussed in detail in Section 4.5.

For all of the four components, a Doppler turbulent velocity  $v_{\text{turb}} = 300 \text{ km s}^{-1}$ , referred to by some as  $b[= \sqrt{2}\sigma = \text{FWHM}/(2\sqrt{\ln 2})]$ , is used (i.e., full width at half-maximum  $\text{FWHM} = 500 \text{ km s}^{-1}$ ), which is approximately the MEG broadening ( $23 \text{ m\AA}$ ) at  $14 \text{ \AA}$ . This value provides a good fit

to the strongest absorption lines in the spectrum. Finally, the model includes also the  $23 \text{ m\AA}$  FWHM instrumental broadening (convolved with the model). The value of  $v_{\text{turb}} = 300 \text{ km s}^{-1}$  is the same value used by Turner et al. (2005) for the slow component. Much narrower lines cannot be resolved in the present spectrum. Turner et al. (2008) used  $v_{\text{turb}} = 200 \text{ km s}^{-1}$  for the slow components while Mehdipour et al. (2010) used  $v_{\text{turb}} = 50 \text{ km s}^{-1}$  for the slowest component and  $v_{\text{turb}} = 400 \text{ km s}^{-1}$  for the second one.

Our model includes all of the important lines of all ion species that can absorb in the HETGS waveband. In the different components of NGC 3516, we find evidence for the following ions:  $\text{N}^{+6}$ ,  $\text{Fe}^{+1}$ – $\text{Fe}^{+25}$ , all oxygen charge states,  $\text{Ne}^{+3}$ – $\text{Ne}^{+9}$ ,  $\text{Mg}^{+4}$ – $\text{Mg}^{+11}$ ,  $\text{Si}^{+5}$ – $\text{Si}^{+13}$ ,  $\text{Ar}^{+16}$ – $\text{Ar}^{+17}$ ,  $\text{Ca}^{+18}$ – $\text{Ca}^{+19}$ , and  $\text{S}^{+14}$ – $\text{S}^{+15}$ . We also include the K-shell photoelectric edges for all these ions although their effect here is largely negligible. When fitting the data, each ionic column density is treated as a free parameter. A preliminary spectral model is obtained using a Monte Carlo fit applied to the entire spectrum. Subsequently, the final fit is obtained for individual ionic column densities in a more controlled manner, which ensures that the fit of the leading lines is not compromised. Ionic column density uncertainties are calculated by varying each column density (while the other ions are fixed) until  $\Delta\chi^2 = 1$ , as described in more detail in Holczer et al. (2007).

The best-fit model is plotted over the data in Figure 4. It can be seen that most ions are reproduced fairly well by the model. Note that some lines could be saturated, e.g., the leading lines of  $\text{O}^{+6}$  and  $\text{O}^{+7}$ . In these cases, the higher order lines with lower oscillator strengths are crucial for obtaining reliable  $N_{\text{ion}}$  values.

### 3.3. AMD Method

The large range of ionization states present in the absorber implies that the absorption arises from gas that is distributed over a wide range of ionization parameter  $\xi$ . Throughout this work, we use the following convention for the ionization parameter  $\xi = L/(n_{\text{H}}r^2)$  in units of  $\text{erg s}^{-1} \text{ cm}$ , where  $L$  is the ionizing luminosity,  $n_{\text{H}}$  is the H number density, and  $r$  is the distance from the ionizing source. We apply the AMD analysis in order to obtain the total hydrogen column density  $N_{\text{H}}$  along the line of sight. The AMD can be expressed as

$$\text{AMD} \equiv \partial N_{\text{H}} / \partial(\log \xi) \quad (3)$$

and

$$N_{\text{H}} = \int \text{AMD} d(\log \xi). \quad (4)$$

The relation between the ionic column densities  $N_{\text{ion}}$  and the AMD is then expressed as

$$N_{\text{ion}} = A_z \int \frac{\partial N_{\text{H}}}{\partial(\log \xi)} f_{\text{ion}}(\log \xi) d(\log \xi), \quad (5)$$

where  $N_{\text{ion}}$  is the measured ion column density,  $A_z$  is the element abundance with respect to hydrogen assumed to be constant throughout the absorber, and  $f_{\text{ion}}(\log \xi)$  is the fractional ion abundance with respect to the total abundance of its element. We aim at recovering the AMD for the different kinematic components of NGC 3516.

For the AMD, we seek a distribution  $\partial N_{\text{H}} / \partial(\log \xi)$  that after integration (Equation (5)) will produce all of the measured ionic column densities. In this procedure, one must take into

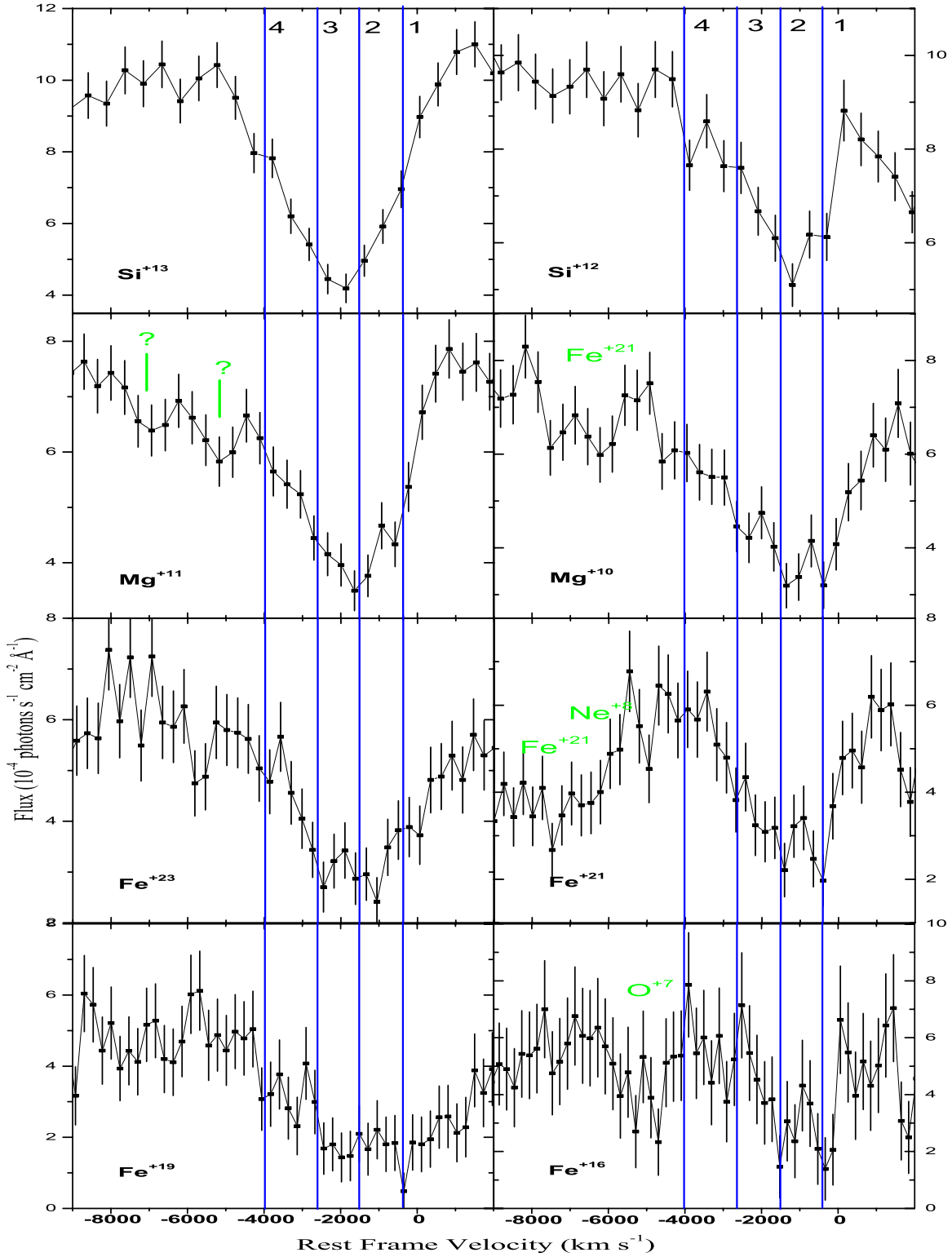


**Figure 3.** *Chandra* HETGS 2006 average spectrum of NGC 3516 in velocity space, corrected for cosmological redshift ( $z = 0.008836$ ) around  $\text{Si}^{+13}$ ,  $\text{Si}^{+12}$ ,  $\text{Mg}^{+11}$ ,  $\text{Mg}^{+10}$ ,  $\text{Fe}^{+23}$ ,  $\text{Fe}^{+21}$ ,  $\text{Fe}^{+19}$ , and  $\text{Fe}^{+16}$  lines. Four kinematic components can be discerned. Other lines are marked in green as are two unidentified troughs next to  $\text{Mg}^{+11}$  (see also Figure 4 at  $8.2 \text{ \AA}$ ). For  $\text{Fe}^{+16}$  only the two slow components are present, which is an indication of the high ionization of the fast components. (A color version of this figure is available in the online journal.)

account the full dependence of  $f_{\text{ion}}$  on  $\xi$ . We employ the XSTAR code (Kallman & Bautista 2001) version 2.1kn3 to calculate  $f_{\text{ion}}(\log \xi)$  using the continuum derived in Section 3.1, and extrapolated to the range of 1–1000 Ryd. During the fit, the AMD bin values are the only parameters left free to vary. The

AMD errors are calculated by varying each bin from its best-fit value while the whole distribution is refitted. This procedure is repeated until  $\Delta\chi^2 = 1$ . The fact that changes in the AMD in one bin can be compensated by varying the AMD in other bins dominates the AMD uncertainties. This is what limits the

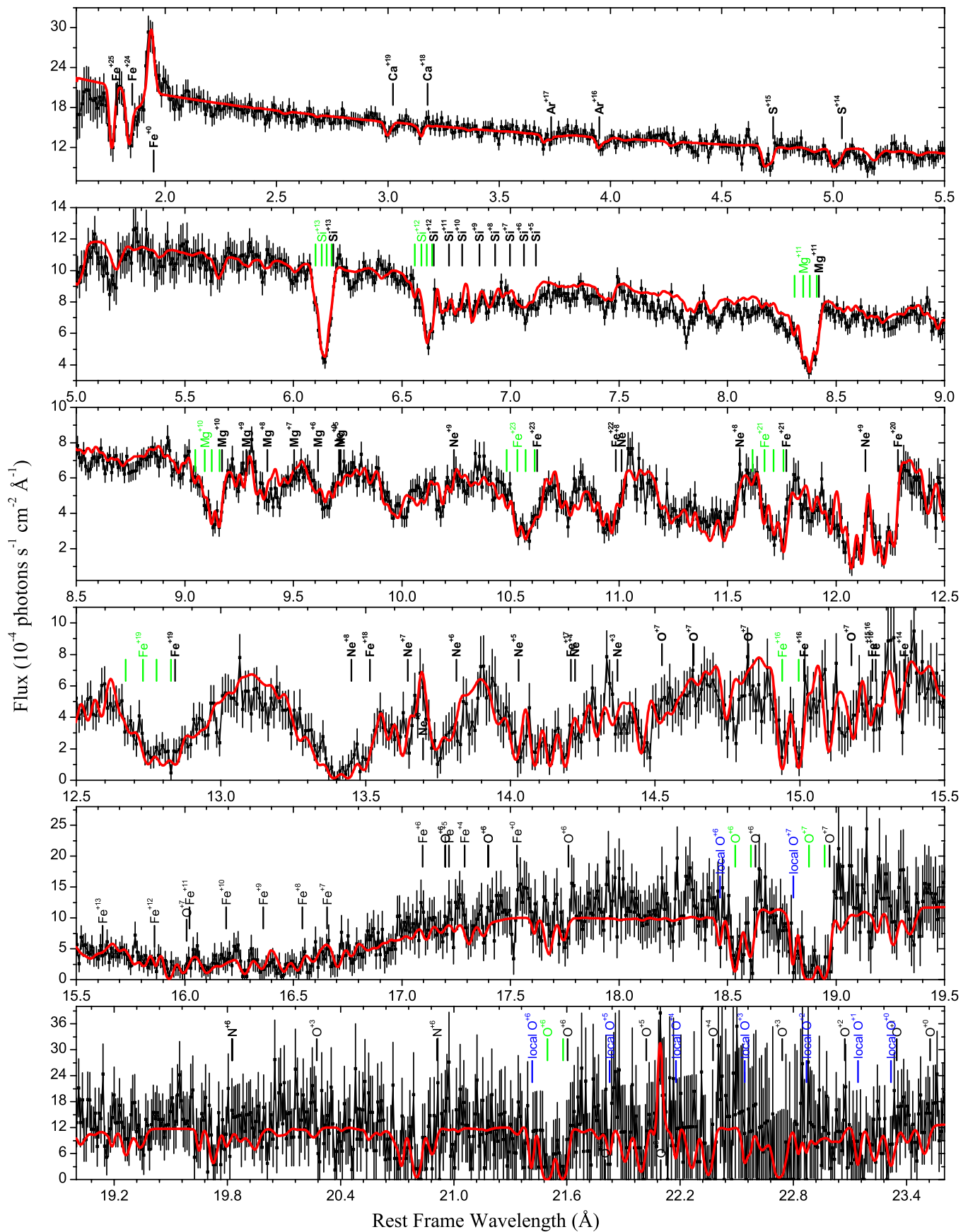


**Figure 4.** *Chandra* HETGS spectrum of NGC 3516 corrected for cosmological redshift ( $z = 0.008836$ ) and binned to 10 m $\text{\AA}$ . The red line is the best-fit model including all four velocity components. Ions producing the strongest absorption (emission) lines and blends are marked above (below) the data. Blue labels represent the local component. Green labels represent the different velocity components for a few prominent lines.

(A color version of this figure is available in the online journal.)

**Table 3**  
Narrow Emission Lines<sup>a</sup>

Line	$\lambda_{\text{Rest}}$ (Å)	$\lambda_{\text{Observed}}^b$ (Å)	Flux ( $10^{-5}$ photon $\text{s}^{-1}$ $\text{cm}^{-2}$ )
Fe <sup>+0</sup> -Fe <sup>+9</sup> K $\alpha$	1.94	1.936 $\pm$ 0.01	3.3 $\pm$ 0.6
Fe <sup>+10</sup> -Fe <sup>+16</sup> K $\alpha$	1.93-1.94 <sup>c</sup>		
Ne <sup>+8</sup> forbidden	13.698	13.69 $\pm$ 0.01	0.5 $\pm$ 0.1
O <sup>+6</sup> forbidden	22.097	22.093 $\pm$ 0.01	6 $\pm$ 1

**Notes.**

<sup>a</sup> FWHM = 235 km  $\text{s}^{-1}$  applied uniformly to oxygen and neon emission lines. FWHM = 3500 km  $\text{s}^{-1}$  was applied to iron K $\alpha$  emission line.

<sup>b</sup> In the AGN rest frame.

<sup>c</sup> Decaux et al. (1995).

number of bins and the AMD resolution in  $\xi$  or  $T$ . Indeed, we choose the narrowest bins (in  $\log \xi$ ) that still give meaningful errors. AMD in neighboring, excessively narrow bins cannot be distinguished by the data, i.e., different narrow-bin distributions produce the measured  $N_{\text{ion}}$  values to within the errors. More details on the AMD binning method and error calculations can be found in Holczer et al. (2007).

The current method obtains a well-defined distribution of ionization, which is tightly constrained by the data, instead of the more traditional method, which constructs a superposition of individual ionization components that are  $\delta$  functions of  $\xi$ , and are obtained through a global-fitting procedure. The current method should not be viewed as an upgraded version of the traditional one. In fact, the two approaches are fundamentally different. While the AMD is a bottom-up approach that uses directly measured quantities  $N_{\text{ion}}$  to derive the distribution, global fitting uses a top-bottom method that imposes a physical model and obtains its best-fit parameters.

The advantage of the AMD method is that it helps identify column density and ionization trends that can then be compared with models (e.g., Fukumura et al. 2010), as well as the precise temperature boundaries between different phases of the possibly multi-phase absorber, e.g., due to thermally unstable temperatures (Holczer et al. 2007). It is not intended to, and indeed does not necessarily provide a superior statistical fit to the spectra.

### 3.4. Narrow Emission Lines

The present NGC 3516 spectrum has a few narrow, bright emission lines. The emission component is added only after the continuum is set and the absorption fit is completed. O<sup>+6</sup> K $\alpha$  and Ne<sup>+8</sup> K $\alpha$  forbidden lines are well fitted with a simple Gaussian broadened by 235 km  $\text{s}^{-1}$  FWHM ( $\sigma = 100$  km  $\text{s}^{-1}$ ) while Fe K $\alpha$  lines were fitted with a broader Gaussian of 3500 km  $\text{s}^{-1}$  FWHM ( $\sigma = 1500$  km  $\text{s}^{-1}$ ). All lines are found to be stationary to within  $\approx 100$  km  $\text{s}^{-1}$ . The centroid wavelength and photon flux are measured for each line and listed in Table 3.

## 4. RESULTS

### 4.1. Ionic Column Densities

The best-fit ionic column densities are listed in Table 4 and the resulting model is plotted over the data in Figure 4. The errors for the ionic column densities were calculated in the same manner as in Holczer et al. (2007). It can be seen that both components 1 and 2 have a wide range of ionization parameter. They both have similar absorption with ionic column densities of the order of  $10^{16}$  to  $10^{17}$   $\text{cm}^{-2}$  in iron, silicon, neon, and

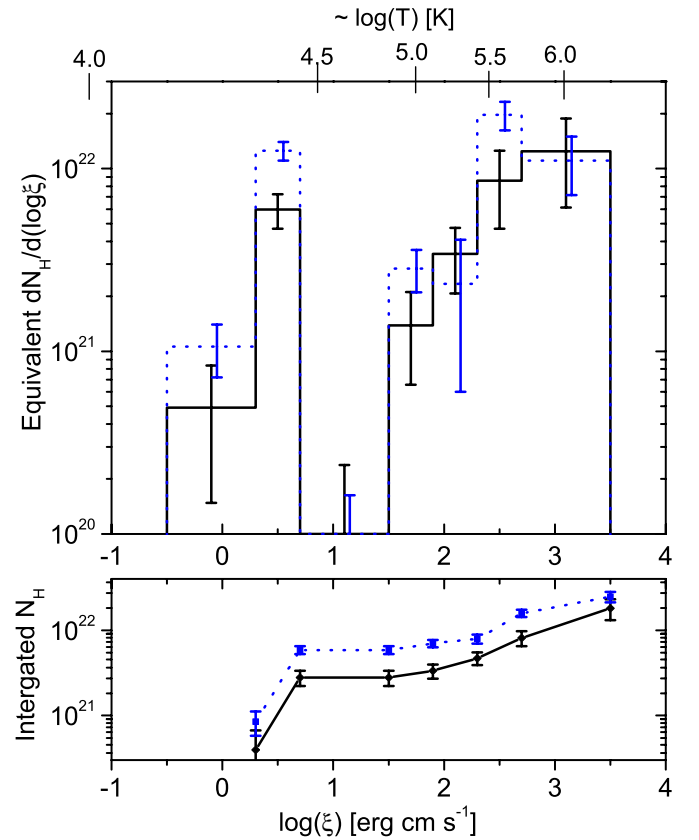


**Figure 5.** AMD of component 1 (solid black) and component 2 (dashed blue) in the outflow of NGC 3516, obtained exclusively from Fe absorption and scaled by the solar Fe/H abundance of  $3.16 \times 10^{-5}$  (Asplund et al. 2009). The corresponding temperature scale, obtained from the XSTAR computation, is shown at the top of the figure. The accumulative column density up to  $\xi$  is plotted in the lower panel, yielding a total of  $N_{\text{H}} = (1.8 \pm 0.5) \times 10^{22}$   $\text{cm}^{-2}$  for component 1 and  $N_{\text{H}} = (2.5 \pm 0.3) \times 10^{22}$   $\text{cm}^{-2}$  for component 2.

(A color version of this figure is available in the online journal.)

magnesium, while those of the more abundant O ions are higher and reach  $\sim 10^{18}$   $\text{cm}^{-2}$ . Components 1 and 2 are similar in the amount of absorption, even though component 2 seems to have slightly higher column densities. Components 3 and 4 consist exclusively of high-ionization species, mostly K-shell ions of Ne, Mg, Si, Fe, S, Ar, and even Ca. In Fe, we detect only the highest ionization L-shell ions in these fast components (see Figure 3).

### 4.2. AMD for Components 1 and 2

The best-fit AMD for components 1 and 2 in NGC 3516 is presented in Figure 5 and the integrated column density is presented in the bottom panel of Figure 5. These AMDs were obtained using 21 charge states of Fe from Fe<sup>+3</sup> through Fe<sup>+23</sup>. K-shell Fe is heavily blended for all the kinematic components (1 through 4); however most of the absorption is due to components 3 and 4. Many M-shell ions are only tentatively detected. Nonetheless, the strict upper limits on so many Fe ions provide tight constraints on the AMD around where these ions form. The result of Figure 5 is enabled by the AMD method and, obviously, cannot be as well quantified with a standard multi- $\xi$  fit. The current integrated AMD of the absorber in NGC 3516 (Figure 5) gives a total column density of  $N_{\text{H}} = (1.8 \pm 0.5) \times 10^{22}$   $\text{cm}^{-2}$  for component 1 and  $N_{\text{H}} = (2.5 \pm 0.3) \times 10^{22}$   $\text{cm}^{-2}$  for component 2.

**Table 4**  
Current Best-fit Column Densities for Ions Detected in the 2006 HETGS Spectrum of NGC 3516

Ion	Column Density $N_{\text{ion}}$ ( $10^{16} \text{ cm}^{-2}$ )		Column Density $N_{\text{ion}}$ ( $10^{16} \text{ cm}^{-2}$ )		Ion	Column Density $N_{\text{ion}}$ ( $10^{16} \text{ cm}^{-2}$ )		Column Density $N_{\text{ion}}$ ( $10^{16} \text{ cm}^{-2}$ )	
	Comp1	Comp2	Comp3	Comp4		Comp1	Comp2	Comp3	Comp4
N <sup>+6</sup>	$10^{+4.0}_{-1}$	$50^{+200}_{-5}$	...	...	S <sup>+14</sup>	$2.0^{+2.3}_{-0.9}$	$3.0^{+0.8}_{-2.1}$	$3.5^{+1.1}_{-2.0}$	...
O <sup>+0</sup>	$8.0^{+2.0}_{-8.0}$	$4.0^{+1.9}_{-4.0}$	...	...	S <sup>+15</sup>	$6.0^{+4.1}_{-1.8}$	$5.0^{+1.9}_{-3.6}$	$8.0^{+7.0}_{-1.5}$	...
O <sup>+1</sup>	$5.0^{+4.2}_{-4.0}$	$6.0^{+2.0}_{-6.0}$	...	...	Ar <sup>+16</sup>	$3.0^{+1.8}_{-1.7}$	...	...	...
O <sup>+2</sup>	$3.0^{+3.9}_{-1.7}$	$2.0^{+4.9}_{-2.0}$	...	...	Ar <sup>+17</sup>	$3.0^{+4.3}_{-2.1}$	...	$5.0^{+6.0}_{-1.8}$	...
O <sup>+3</sup>	$11^{+3}_{-11}$	$2.0^{+2.7}_{-2.0}$	...	...	Ca <sup>+18</sup>	...	...	$5.0^{+2.6}_{-2.9}$	...
O <sup>+4</sup>	$5.0^{+1.1}_{-5.0}$	$3.0^{+0.7}_{-3.0}$	...	...	Ca <sup>+19</sup>	$2.0^{+6.6}_{-2.0}$	$4.0^{+4.0}_{-4.0}$	$8.0^{+4.3}_{-5.0}$	...
O <sup>+5</sup>	$4.0^{+1.4}_{-3.7}$	$2.0^{+0.4}_{-2.0}$	...	...	Fe <sup>+1</sup>	$0.2^{+0.4}_{-0.2}$	$0.2^{+0.4}_{-0.2}$	...	...
O <sup>+6</sup>	$10^{+9.0}_{-1.0}$	$20^{+8.0}_{-2.0}$	...	...	Fe <sup>+2</sup>	$0.2^{+0.3}_{-0.2}$	$0.2^{+0.3}_{-0.2}$	...	...
O <sup>+7</sup>	$18^{+300}_{-2}$	$100^{+300}_{-10}$	...	...	Fe <sup>+3</sup>	$0.2^{+0.3}_{-0.2}$	$0.2^{+0.3}_{-0.2}$	...	...
Ne <sup>+3</sup>	$1.0^{+1.9}_{-1.0}$	$4.0^{+4.0}_{-2.0}$	...	...	Fe <sup>+4</sup>	$0.2^{+0.2}_{-0.2}$	$0.2^{+0.4}_{-0.2}$	...	...
Ne <sup>+4</sup>	$3.0^{+5.5}_{-1.0}$	$0.5^{+3.2}_{-0.5}$	...	...	Fe <sup>+5</sup>	$0.2^{+0.3}_{-0.2}$	$0.2^{+0.3}_{-0.2}$	...	...
Ne <sup>+5</sup>	$4.0^{+1.7}_{-2.5}$	$3.0^{+0.8}_{-2.5}$	...	...	Fe <sup>+6</sup>	$0.2^{+0.3}_{-0.2}$	$0.2^{+0.3}_{-0.2}$	...	...
Ne <sup>+6</sup>	$1.0^{+1.3}_{-0.9}$	$2.0^{+6.0}_{-0.4}$	...	...	Fe <sup>+7</sup>	$0.5^{+2.1}_{-0.1}$	$2.0^{+1.7}_{-0.3}$	...	...
Ne <sup>+7</sup>	$4.0^{+4.9}_{-0.8}$	$2.0^{+1.1}_{-1.0}$	...	...	Fe <sup>+8</sup>	$1.0^{+1.0}_{-0.3}$	$2.0^{+2.7}_{-0.3}$	...	...
Ne <sup>+8</sup>	$4.0^{+18}_{-0.4}$	$6.0^{+25}_{-0.6}$	$2.0^{+2.0}_{-0.2}$	...	Fe <sup>+9</sup>	$1.0^{+5.1}_{-0.2}$	$3.8^{+1.7}_{-0.7}$	...	...
Ne <sup>+9</sup>	$7^{+30}_{-0.4}$	$13^{+50}_{-1.3}$	$7.0^{+30}_{-0.7}$	$4.0^{+18}_{-0.6}$	Fe <sup>+10</sup>	$0.5^{+1.7}_{-0.4}$	$4.0^{+1.7}_{-0.6}$	...	...
Mg <sup>+4</sup>	$0.5^{+2.4}_{-0.5}$	$0.5^{+1.1}_{-0.5}$	...	...	Fe <sup>+11</sup>	$1.7^{+0.8}_{-0.7}$	$1.4^{+1.2}_{-0.6}$	...	...
Mg <sup>+5</sup>	$0.5^{+0.8}_{-0.5}$	$0.5^{+6.8}_{-0.2}$	...	...	Fe <sup>+12</sup>	$1.0^{+1.0}_{-0.2}$	$2.0^{+0.4}_{-0.7}$	...	...
Mg <sup>+6</sup>	$1.5^{+2.5}_{-0.4}$	$0.9^{+3.7}_{-0.3}$	...	...	Fe <sup>+13</sup>	$0.5^{+0.3}_{-0.4}$	$1.0^{+0.3}_{-0.4}$	...	...
Mg <sup>+7</sup>	$1.5^{+3.0}_{-0.2}$	$0.8^{+5.2}_{-0.1}$	...	...	Fe <sup>+14</sup>	$0.5^{+0.1}_{-0.4}$	$0.5^{+0.2}_{-0.2}$	...	...
Mg <sup>+8</sup>	$2.0^{+2.9}_{-0.2}$	$2.0^{+0.5}_{-0.6}$	...	...	Fe <sup>+15</sup>	$0.2^{+0.4}_{-0.2}$	$0.5^{+1.3}_{-0.1}$	...	...
Mg <sup>+9</sup>	$2.0^{+1.8}_{-0.3}$	$1.5^{+3.5}_{-0.2}$	...	...	Fe <sup>+16</sup>	$2.4^{+0.5}_{-0.5}$	$2.5^{+1.6}_{-0.3}$	...	...
Mg <sup>+10</sup>	$4.0^{+9.4}_{-0.4}$	$4.0^{+20}_{-0.4}$	$2.0^{+8.0}_{-0.2}$	$1.0^{+3.2}_{-0.1}$	Fe <sup>+17</sup>	$2.5^{+0.2}_{-2.2}$	$2.5^{+0.6}_{-0.7}$	$3.0^{+0.5}_{-0.7}$	$1.5^{+1.6}_{-0.2}$
Mg <sup>+11</sup>	$5.5^{+1.9}_{-0.6}$	$9.0^{+5.6}_{-0.4}$	$6.5^{+3.7}_{-0.7}$	$2.5^{+2.8}_{-0.3}$	Fe <sup>+18</sup>	$5.0^{+0.5}_{-1.2}$	$6.0^{+1.6}_{-0.5}$	$4.4^{+0.8}_{-0.7}$	$1.3^{+0.8}_{-0.4}$
Si <sup>+5</sup>	$3.0^{+10}_{-0.8}$	$4.0^{+9.4}_{-0.8}$	...	...	Fe <sup>+19</sup>	$3.6^{+1.0}_{-0.4}$	$3.9^{+2.4}_{-0.4}$	$4.2^{+1.1}_{-0.5}$	$2.0^{+0.6}_{-0.2}$
Si <sup>+6</sup>	$3.0^{+3.2}_{-0.8}$	$4.0^{+4.5}_{-0.6}$	...	...	Fe <sup>+20</sup>	$2.2^{+2.2}_{-0.2}$	$3.5^{+8.8}_{-0.4}$	$2.8^{+9.6}_{-0.3}$	$1.0^{+2.4}_{-0.2}$
Si <sup>+7</sup>	$2.0^{+4.7}_{-0.3}$	$3.0^{+2.3}_{-0.6}$	...	...	Fe <sup>+21</sup>	$3.0^{+3.0}_{-0.3}$	$3.5^{+4.5}_{-0.4}$	$2.7^{+3.5}_{-0.3}$	$0.7^{+2.7}_{-0.1}$
Si <sup>+8</sup>	$3.0^{+2.8}_{-0.3}$	$4.0^{+2.7}_{-0.4}$	...	...	Fe <sup>+22</sup>	$3.0^{+3.7}_{-0.3}$	$3.0^{+7.9}_{-0.3}$	$3.0^{+4.5}_{-0.3}$	$0.5^{+1.0}_{-0.3}$
Si <sup>+9</sup>	$2.0^{+1.2}_{-0.4}$	$5.0^{+0.6}_{-0.9}$	...	...	Fe <sup>+23</sup>	$0.3^{+8.0}_{-0.2}$	$4.0^{+12}_{-0.4}$	$8.0^{+4.5}_{-0.8}$	$2.0^{+0.6}_{-2.0}$
Si <sup>+10</sup>	$2.6^{+0.6}_{-0.5}$	$2.9^{+1.0}_{-0.3}$	...	...	Fe <sup>+24</sup>	$0.1^{+40}_{-0.1}$	$30^{+70}_{-12}$	$22^{+66}_{-14}$	$20^{+25}_{-13}$
Si <sup>+11</sup>	$2.5^{+0.8}_{-0.5}$	$2.8^{+2.0}_{-0.3}$	...	...	Fe <sup>+25</sup>	$0.1^{+50}_{-0.1}$	$10^{+70}_{-10}$	$60^{+150}_{-20}$	$130^{+500}_{-36}$
Si <sup>+12</sup>	$4.5^{+0.9}_{-0.7}$	$7.0^{+1.8}_{-0.7}$	$1.5^{+2.5}_{-0.2}$	$1.5^{+0.9}_{-0.4}$					
Si <sup>+13</sup>	$4.7^{+4.3}_{-0.4}$	$15^{+7.7}_{-1.5}$	$14^{+6.8}_{-1.4}$	$5.0^{+3.4}_{-0.5}$					

Both AMDs feature a statistically significant minimum at  $0.7 < \log \xi < 1.5$  ( $\text{erg s}^{-1} \text{ cm}$ ), which corresponds to temperatures  $4.5 < \log T < 5$  (K). This discontinuity in the AMD at the same temperatures was also observed in IRAS 13349+2438, NGC 3783 (Holczer et al. 2007), NGC 7469 (Blustin et al. 2007), and MCG –6–30–15 (Holczer et al. 2010). Indeed, the multi-phase nature of AGN outflows is found in many warm absorbers (Sako et al. 2001; Krongold et al. 2003, 2005, 2007; Detmers et al. 2011). It is mostly a manifestation of the relatively low ionic column densities observed for the ions Fe<sup>+11</sup>–Fe<sup>+15</sup>, as can be seen in Table 4. One way to explain this gap is that this temperature regime is thermally unstable (Holczer et al. 2007; Gonçalves et al. 2010). Gas at  $4.5 < \log T < 5$  (K) could be unstable as the cooling function

$\Lambda(T)$  generally decreases with temperature in this regime. Such instabilities could result in a multi-phase (hot and cold) plasma in pressure equilibrium, as suggested by Krolik et al. (1981).

It is somewhat surprising that the AMDs of components 1 and 2 are so similar, which implies the physical conditions in components 1 and 2, the distance from the source and the outflow density, as well as the overall outflow column are similar. Given the similar AMDs we are led to think that these components are connected. What about the faster components 3 and 4? Are they also connected to components 1 and 2? Components 3 and 4 have yet to be reported, so no comparisons can be made with other authors. These new components and a plausible geometric explanation are addressed in detail in Section 4.7, while their ionization distributions are discussed below.

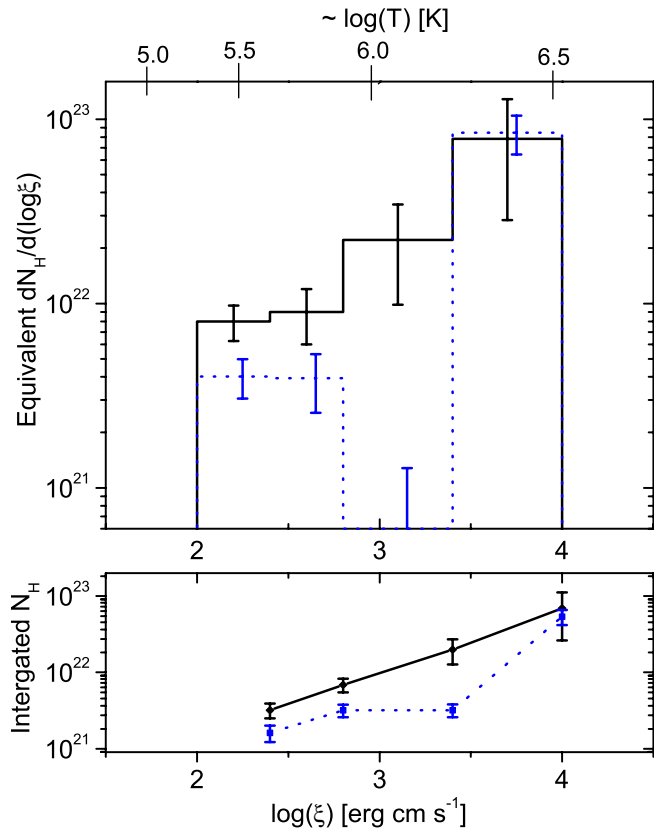


**Figure 6.** AMD of component 3 (black) and component 4 (dashed blue) in the outflow of NGC 3516 obtained exclusively from Fe absorption and scaled by the solar Fe/H abundance of  $3.16 \times 10^{-5}$  (Asplund et al. 2009). The corresponding temperature scale, obtained from the XSTAR computation, is shown at the top of the figure. The accumulative column density up to  $\xi$  is plotted in the lower panel, yielding a total of  $N_{\text{H}} = (6.9 \pm 4.3) \times 10^{22} \text{ cm}^{-2}$  for component 3 and  $N_{\text{H}} = (5.4 \pm 1.2) \times 10^{22} \text{ cm}^{-2}$  for component 4.

(A color version of this figure is available in the online journal.)

#### 4.3. AMD for Components 3 and 4

The best-fit AMD for components 3 and 4 in NGC 3516 is presented in Figure 6 and the integrated column density is presented in the bottom panel of Figure 6. The black line represents component 3 while the blue dotted line represents component 4. These AMDs were obtained using L-shell and K-shell charge states of Fe only as no M-shell Fe ions are detected, which is why these AMDs begin at  $\log \xi = 2$  ( $\text{erg s}^{-1} \text{ cm}$ ). On the other hand, the AMD value of these components for  $\log \xi > 2$  ( $\text{erg s}^{-1} \text{ cm}$ ) is an order of magnitude higher than in components 1 and 2. In the K-shell Fe lines, all the components are blended; however the troughs are dominated by components 3 and 4. It can be seen that both AMDs show similar shape but component 4 has a minimum at  $2.8 \leq \log \xi \leq 3.4$  ( $\text{erg s}^{-1} \text{ cm}$ ), mostly due to the low columns of  $\text{Fe}^{+20}$ – $\text{Fe}^{+22}$ , as can be seen in Table 4. Similarly to components 1 and 2, we are led to think that components 3 and 4 are also connected; particularly since they both appear in the 2006 spectrum, but are both absent in the 2001 spectrum (see Section 4.6). The total column density (integrated AMD) gives  $N_{\text{H}} = (6.9 \pm 4.3) \times 10^{22} \text{ cm}^{-2}$  for component 3 and  $N_{\text{H}} = (5.4 \pm 1.2) \times 10^{22} \text{ cm}^{-2}$  for component 4.

#### 4.4. Total Column Density

In order to further compare our results with previous outflow models for NGC 3516, we can formally rebin the AMD in

Figure 5 to two regions, one below  $\log \xi < 0.5$  and one above  $\log \xi > 1.5$  (this process is done to each kinematic component). The physical parameters of these two ionization regions are subsequently compared with all previous works in Table 5.

The total column density that we find for the low velocity  $-350 \text{ km s}^{-1}$  component 1 is roughly  $2 \times 10^{22} \text{ cm}^{-2}$  and is comparable to that of Kriss et al. (1996b) (their components 1 and 2). Most other works are consistent with this result to within a factor of two (Reynolds 1997; Mathur et al. 1997; Netzer et al. 2002; Turner et al. 2005, 2008; Mehdipour et al. 2010). However, if the Costantini et al. (2000) hot component also refers to our component 1, then there is a larger disagreement of around an order of magnitude.

Component 2 ( $v = -1500 \text{ km s}^{-1}$ ) was detected only with the more recent grating instruments. The column density we find for component 2 is in good agreement with the Turner et al. (2005) “High” component and the Mehdipour et al. (2010) component “B” and still consistent with the weak constraints of Markowitz et al. (2008) “Zone 3” and “Zone 4” and the Turner et al. (2005) “Heavy” component. We should note that both Turner et al. (2008) and Mehdipour et al. (2010) used another component with an intermediate outflow velocity ( $\sim -1000 \text{ km s}^{-1}$ ), namely “Zone 4” and component “C,” respectively. Table 5 shows that the total column density can vary between observations and authors by nearly two orders of magnitude. The highest column densities are due to few spectral features, e.g., Fe–K in the present work, or to the need to explain spectral curvature with photoelectric absorption without lines (Turner et al. 2008). The diversity in ionization parameter and velocity is mostly due to selective identification of spectral features. Our analysis shows that a broad range of both ionization and velocity are present.

#### 4.5. Possible Local Absorption

The outflow velocity of component 3 is  $-2600 \pm 200 \text{ km s}^{-1}$  matching the cosmological recession of  $-2650 \text{ km s}^{-1}$ , which raises the possibility that some of the absorption at this velocity is due to local absorption as commonly found along lines of sight to bright AGNs (e.g., Nicastro et al. 2003; Williams et al. 2005). A similar component was recently found in MCG  $-6-30-15$  (Holczer et al. 2010), although there it was kinematically resolved ( $-1900 \pm 150 \text{ km s}^{-1}$  versus  $-2300 \text{ km s}^{-1}$ ). The oxygen and nitrogen lines of component 3 are narrow and thus suspect of having a local origin. These lines require  $v_{\text{turb}} = 100 \text{ km s}^{-1}$  (FWHM =  $170 \text{ km s}^{-1}$ ), which is less than  $v_{\text{turb}} = 300 \text{ km s}^{-1}$ , which is used for higher ionization. This narrow width is consistent with local, ionized interstellar medium (ISM) UV absorption lines along this line of sight (Kraemer et al. 2002). There are a few additional reasons to favor the local component scenario for O and N. First, they form at lower ionization parameters of  $\log \xi \sim 0-2$ , while most of component 3 is primarily comprised of high ionization species. In Fe, we do not detect any M-shell ions, and not even  $\text{Fe}^{+16}$  in this component. Even though we cannot conclusively determine whether the oxygen and nitrogen absorption comes from outflow component 3, or has a local origin, we tend to favor the local origin scenario because such a component is often observed.

The (presumably) local component column densities are shown in Table 6. The low charge states are due to the Galactic disk and halo, and likely not associated with the higher ionization states that are due to the hot phase of the Galactic halo or the Local Group. The oxygen ionic column densities are all in the range of several  $10^{16} \text{ cm}^{-2}$ , which implies a

**Table 5**  
Physical Parameters for Absorption Components in Order  
of Outflow Velocity: Comparison

Ref. <sup>a</sup>	Observatory	Component	Outflow Velocity (km s <sup>-1</sup> )	Column Density (10 <sup>21</sup> cm <sup>-2</sup> )	Total Column Density (10 <sup>21</sup> cm <sup>-2</sup> )	Ionization Parameter log $\xi$ (erg s <sup>-1</sup> cm)
1	ASCA	1	<-120	14.1 ± 3.9	21 ± 4	1.66 ± 0.31 <sup>b</sup>
		2	<-120	6.9 ± 0.6		0.32 ± 0.11 <sup>b</sup>
2	ASCA	...	...	10.0 <sup>+1.1</sup> <sub>-1.6</sub>	10 ± 1	1.44 ± 0.03
3	ROSAT	...	-500	7 ± 1	7 ± 1	0.90-1.11 <sup>b</sup>
4 <sup>d</sup>	BeppoSAX	Warm	-500	10 ± 0.4	168 ± 73	0.73 ± 0.10 <sup>b</sup>
		Hot	-500	158 ± 73		2.36 ± 0.10 <sup>b</sup>
5 <sup>e</sup>	ASCA	...	...	8	8	-2.6 <sup>c</sup>
6	XMM-Newton Chandra	UV	-200	6 ± 2	272 ± 23	-0.5
		High	-1100	16		2.5
		Heavy	-1100	250 ± 23		3.0
7	Suzaku	Primary	...	55 ± 2	95 ± 45	0.3 ± 0.1
		High Ion.	-1100	40 <sup>+46</sup> <sub>-31</sub>		3.7 <sup>+0.3</sup> <sub>-0.7</sub>
		Zone 1	...	2.4 <sup>+0.3</sup> <sub>-0.2</sub>		467 ± 110
8	XMM-Newton Chandra	Zone 2	...	0.5 ± 0.1	34	0.25
		Zone 4	-1000	262 <sup>+63</sup> <sub>-87</sub>		4.31 <sup>+1.19</sup> <sub>-0.14</sub>
		Zone 3	-1600	202 <sup>+87</sup> <sub>-32</sub>		2.19 ± 0.07
9	XMM-Newton	A	-100	4	34	0.9
		C	-900	10		3.0
		B	-1500	20		2.4
10	Chandra	Comp 1	-350 ± 100	2.8 ± 0.6	166 ± 45	-0.5-0.7
			-350 ± 100	15.3 ± 5.0		1.5-3.5
		Comp 2	-1500 ± 150	5.9 ± 0.6		-0.5-0.7
			-1500 ± 150	18.8 ± 3.5		1.5-3.5
		-2600 ± 200	69 ± 43	2-4		
		-4000 ± 400	54 ± 12	2-4		

**Notes.**

- <sup>a</sup> (1) Kriss et al. 1996b; (2) Reynolds 1997; (3) Mathur et al. 1997; (4) Costantini et al. 2000; (5) Netzer et al. 2002; (6) Turner et al. 2005; (7) Markowitz et al. 2008; (8) Turner et al. 2008; (9) Mehdipour et al. 2010; (10) present work.  
<sup>b</sup> Ionization parameter used is  $U$ .  
<sup>c</sup> Ionization parameter used is  $U_{\text{Ox}}$ .  
<sup>d</sup> Reference to data set 97BF therein.  
<sup>e</sup> Reference to data set ASCA98 therein.

**Table 6**  
Oxygen and Nitrogen Ionic Column Densities at  $z = 0$

Charge State	$N_{\text{ion}}$ Local (10 <sup>16</sup> cm <sup>-2</sup> )	$\lambda_{\text{Rest}}$ (Å)
N <sup>+6</sup>	20 <sup>+50</sup> <sub>-2</sub>	19.825,20.911
Neutral O	4.0 <sup>+8.0</sup> <sub>-4</sub>	23.523
O <sup>+1</sup>	6.0 <sup>+20</sup> <sub>-2.7</sub>	23.347
O <sup>+2</sup>	4.0 <sup>+11</sup> <sub>-3.8</sub>	23.071
O <sup>+3</sup>	3.0 <sup>+1.3</sup> <sub>-3.0</sub>	22.741
O <sup>+4</sup>	1.5 <sup>+1.5</sup> <sub>-1.5</sub>	22.374
O <sup>+5</sup>	1.0 <sup>+0.6</sup> <sub>-1.0</sub>	22.019
O <sup>+6</sup>	5 <sup>+20</sup> <sub>-0.5</sub>	21.602
O <sup>+7</sup>	10 <sup>+40</sup> <sub>-1</sub>	18.969

neutral hydrogen column density of a few 10<sup>20</sup> cm<sup>-2</sup>, using  $4.9 \times 10^{-4}$  for the O to H ratio (Asplund et al. 2009) and a fractional ionic abundance of 0.5. This value is consistent with the Galactic absorption of  $N_{\text{H}} = 3.23 \times 10^{20}$  cm<sup>-2</sup> (Dickey & Lockman 1990). Using the same calculations for N<sup>+6</sup> gives a slightly higher neutral hydrogen column density of the order of  $\sim 10^{21}$  cm<sup>-2</sup>.

Note that most species of component 3 are likely not local since their ionization and column densities are too high. Ions

such as Fe<sup>+23-+25</sup>, K-shell S and Si (see Table 4) are usually not observed in the local ionized ISM. Moreover, the high column density measured in this component of  $N_{\text{H}} \sim 10^{23}$  cm<sup>-2</sup> is far higher than typical local ISM columns.

#### 4.6. Variability

The observation of 2006 caught NGC 3516 in a much higher state than the 2001 observation, as can be seen in Figure 2. So far, the analysis in this paper has focused on the 2006 observation. We now want to use the two flux states to study the differences between the two. Several explanations for the flux and spectral variability of NGC 3516 can be found in the literature. Netzer et al. (2002) reported a slow, monotonic decay in flux between 1994 and 2000; however BeppoSAX observations from 1996 and 1997 as well as the present data show a sharp transition between high and low flux over a period of four months (see Table 1). Turner et al. (2005, 2008) used a varying covering factor. However, Mehdipour et al. (2010) found that a varying covering factor did not fit the data, while a variable source continuum could.

In order to compare the absorption in 2001 and 2006 we scaled up the 2001 spectrum to the flux level of 2006 near specific lines. Since absorption depends exponentially on optical depth, this comparison shows changes in optical depth directly, independent of continuum flux. If the absorber did not change,

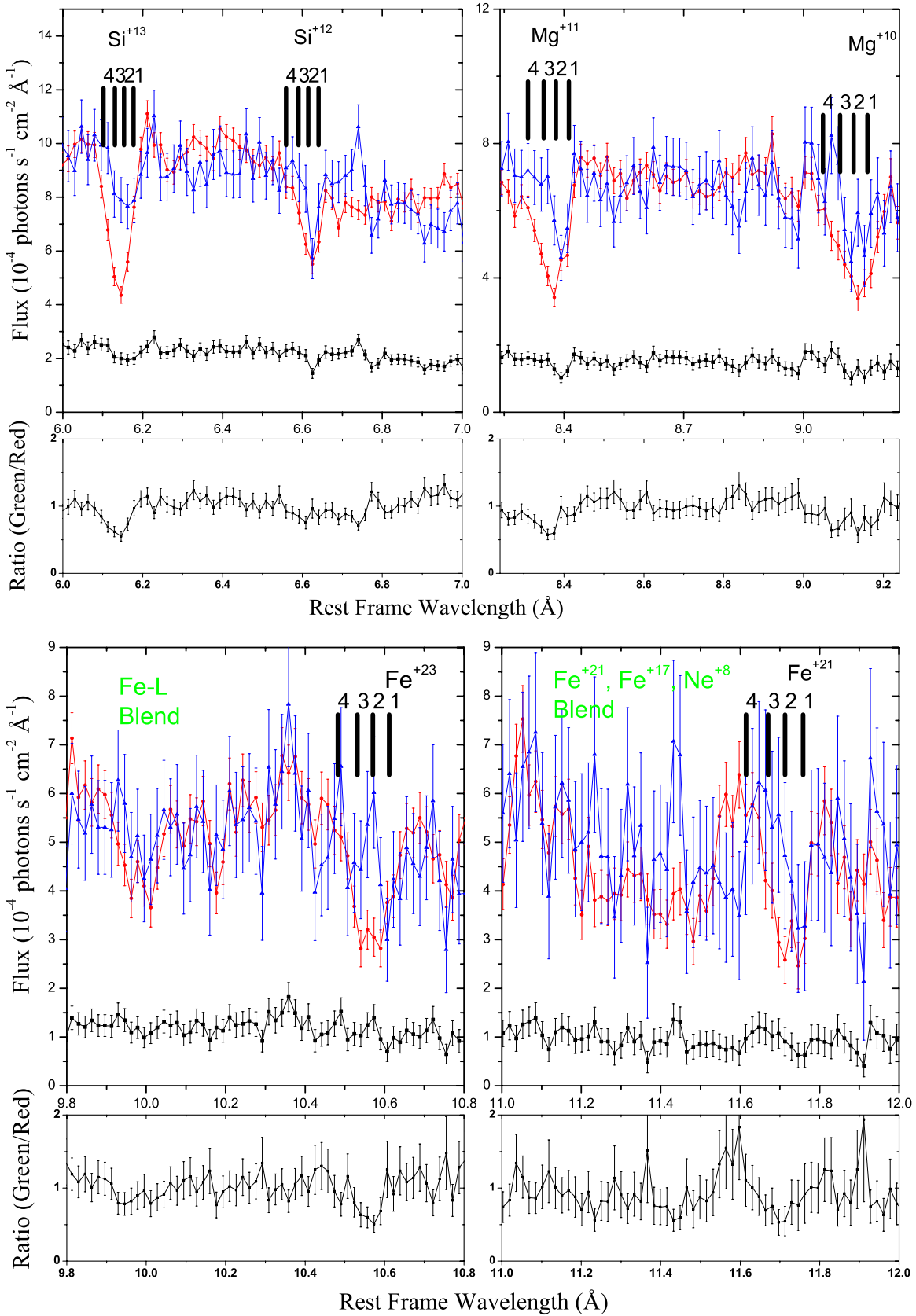


**Figure 7.** *Chandra* HETGS spectrum of NGC 3516 corrected for cosmological redshift ( $z = 0.008836$ ) around K-shell Si (upper left panel), K-shell Mg (upper right panel), Fe<sup>+23</sup> (lower left panel), and Fe<sup>+21</sup> (lower right panel) lines. The black and red spectra represent the combined observations of 2001 and 2006, respectively. The blue data represent the 2001 spectrum scaled up to match the 2006 continuum. The four kinematic components are labeled. The spectral lines in the 2001 data lack absorption in the fast component that is present in 2006. The lower panels are the ratios between the 2006 and 2001 scaled spectra.

(A color version of this figure is available in the online journal.)

the scaled-up trough should match that of the high state. Because the continuum shape during the two states is different, this comparison is meaningful only locally. Indeed, we show this comparison around the most prominent lines. Results for Si and Mg  $K\alpha$  lines and for  $\text{Fe}^{+23}$  and  $\text{Fe}^{+21}$  are shown in Figure 7, where the low statistics spectrum is multiplied by 4 in the upper left panel, by 4.5 in the upper right panel, by 4.3 in the lower left panel, and by 5.2 in the lower right panel. The signal-to-noise ratio (S/N) in the low state is worse, but it appears that component 1 (the slowest component) did not change much between the high and low states. On the other hand, some of component 2 and most of components 3 and 4 are absent in the 2001 low state. In the next section, we discuss a possible geometrical explanation for this result.

#### 4.7. Possible Geometry of Outflow

We find that, apart from a lower continuum level, the 2001 spectrum of NGC 3516 also lacks the faster absorption components. The appearance of high ionization ( $\log \xi \sim 3.5$  erg  $\text{s}^{-1}$  cm) components with columns of  $N_{\text{H}} \sim 10^{23}$   $\text{cm}^{-2}$  is reminiscent of the variable covering invoked by Turner et al. (2005, 2008) to explain the varying continuum shape. We allude to three other possible explanations.

1. *Photoionization change.* The faster components of the outflow are also more ionized. One possibility could be that the fast components recombined due to the reduced flux and are thus not seen in 2001. However, one would still expect to observe the fast components in lower charge states. We could not detect the fast components in the 2001 spectrum in any ion. Since the 2001 spectrum has a much lower S/N, we cannot unambiguously rule out this possibility.
2. *Fast components crossing line of sight.* Another possibility could be that the fast components, while not in the line of sight in 2001, passed through our line of sight in 2006: 5 years are plenty of time, compared to the variability timescale of months that perhaps represents the size of the source, to make this scenario work. Such transverse velocities have been proposed for NGC 4151 by Kraemer et al. (2006). Recent simulations show this behavior of disappearing fast absorbing component explicitly on a similar timescale of few years (Sim et al. 2010, Figure 7).
3. *Lighting up the disk.* The third possibility is that the fast components are present the whole time, but in 2001, when the flux is low, there was no light from the accretion disk behind them for them to absorb. In 2006, the source flux is much brighter, whether intrinsic source output change or flux change due to variable covering factor by thick gas, which could result from a flare on the disk that illuminates the fast components from behind, and which subsequently they absorb along the line of sight.

With the current spectra, one cannot rule out any of these scenarios. With better S/N spectra, one might be able to confirm (or rule out) changes in the (photo)ionization state if the fast component is detected (or not detected) in low ionization species during the low flux state. If one would detect a change in the covering fraction in the narrow absorption lines, which we are not able to detect here, that would be evidence for transverse velocities (Kraemer et al. 2006). The possibility of flaring on the disk is most difficult to test, as the angular resolution required for detecting sources on sub-disk scales is currently prohibitive.

## 5. CONCLUSIONS

We have analyzed the kinematic and thermal structure of the ionized outflow in NGC 3516. We find absorption troughs in dozens of charge states that extend from zero to almost 5000  $\text{km s}^{-1}$ . We model the outflow with four absorption systems. The first and second components are outflowing at  $-350$  and  $-1500$   $\text{km s}^{-1}$ , and span a considerable range of ionization from at least  $\text{Fe}^{+1}$  to  $\text{Fe}^{+23}$  ( $-0.5 < \log \xi < 3.5$  (erg  $\text{s}^{-1}$  cm)). The third and fourth components are outflowing at  $-2600$  and  $-4000$   $\text{km s}^{-1}$ , respectively, and are highly ionized featuring only L-shell and K-shell iron and K-shell ions from lighter elements. Finally, a component of local absorption at  $z = 0$  ( $-2630$   $\text{km s}^{-1}$ ) is detected: this component could be part of the third component; however its low ionization and narrow time profiles imply it is more likely at  $z = 0$ .

Using our AMD reconstruction method for all four components, we measured the distribution of column density as a function of  $\xi$ . We find a double-peaked distribution with a significant minimum at  $0.7 < \log \xi < 1.5$  (erg  $\text{s}^{-1}$  cm) in components 1 and 2, which corresponds to temperatures of  $4.5 < \log T < 5$  (K). This minimum was observed in other AGN outflows like MCG  $-6-30-15$ , NGC 3783, IRAS 13349+2438, and NGC 7469, and it can be ascribed to thermal instability that appear to exist ubiquitously in photoionized Seyfert winds. The AMD of component 3 shows a continuous rise in column density toward higher ionization parameters. The AMD of component 4 is similar in some aspects to that of component 3; however it shows a minimum at  $\log T \sim 6$  (K) mostly due to low  $\text{Fe}^{+20}$ – $\text{Fe}^{+22}$  column densities. The local absorption system could arise from either the ionized Galactic ISM or from the Local Group. The fast components 3 and 4 are not present in the lower flux spectra of 2001.

We thank Shai Kaspi for useful comments. This work was supported by a grant from the ISF.

## REFERENCES

- Asplund, M., Grevesse, N., Sauval, A. J., & Scott, P. 2009, *ARA&A*, 47, 481
- Bar-Shalom, A., Klapisch, M., & Oreg, J. 2001, *J. Quant. Spectrosc. Radiat. Transfer*, 71, 169
- Behar, E. 2009, *ApJ*, 703, 1346
- Behar, E., Cottam, J. C., & Kahn, S. M. 2001a, *ApJ*, 548, 966
- Behar, E., & Netzer, H. 2002, *ApJ*, 570, 165
- Behar, E., Rasmussen, A. P., Blustin, A. J., et al. 2003, *ApJ*, 598, 232
- Behar, E., Sako, M., & Kahn, S. M. 2001b, *ApJ*, 563, 497
- Blustin, A. J., Kriss, G. A., Holczer, T., Behar, E., & Kaastra, J. S. 2007, *A&A*, 466, 107
- Chelouche, D. 2008, arXiv:0812.3621
- Costantini, E., Nicastro, F., Fruscione, A., et al. 2000, *ApJ*, 544, 283
- Crenshaw, D. M., Kraemer, S. B., Boggess, A., et al. 1999, *ApJ*, 516, 750
- Crenshaw, D. M., Kraemer, S. B., & George, I. M. 2003, *ARA&A*, 41, 117
- Decaux, V., Beiersdorfer, P., Osterheld, A., Chen, M., & Kahn, S. M. 1995, *ApJ*, 443, 464
- Detmers, R. G., Kaastra, J. S., Steenbrugge, K. C., et al. 2011, *A&A*, 534, A38
- Dickey, J. M., & Lockman, F. J. 1990, *ARA&A*, 28, 215
- Fukumura, K., Kazanas, D., Behar, E., & Contopoulos, I. 2011, *BAAS*, 43, 327.17
- Fukumura, K., Kazanas, D., Contopoulos, I., & Behar, E. 2010, *ApJ*, 715, 636
- Gonçalves, A. C., Goosmann, R. W., Mouchet, M., et al. 2010, in *AIP Conf. Proc.* 1248, X-Ray Astronomy 2009, Present Status, Multi-Wavelength Approach And Future Perspectives, ed. A. Comastri, L. Argelini, & M. Cappi (Melville, NY: AIP), 439
- Gu, M. F., Holczer, T., Behar, E., & Kahn, S. M. 2006, *ApJ*, 641, 1227
- Haardt, F., Galli, M. R., Treves, A., et al. 2001, *ApJS*, 133, 187
- Halpern, J. P. 1984, *ApJ*, 281, 90
- Holczer, T., Behar, E., & Arav, N. 2010, *ApJ*, 708, 981

- Holczer, T., Behar, E., & Kaspi, S. 2005, *ApJ*, **632**, 788  
Holczer, T., Behar, E., & Kaspi, S. 2007, *ApJ*, **663**, 799  
Kallman, T. R., & Bautista, M. 2001, *ApJS*, **133**, 221  
Kaspi, S., Brandt, W. N., Netzer, H., et al. 2001, *ApJ*, **554**, 216  
Keel, W. C. 1996, *AJ*, **111**, 696  
Kolman, M., Halpern, J. P., Martin, C., Awaki, H., & Koyama, K. 1993, *ApJ*, **403**, 592  
Kraemer, S. B., Crenshaw, D. M., Gabel, J. R., et al. 2006, *ApJS*, **167**, 161  
Kraemer, S. B., Crenshaw, D. M., George, I. M., et al. 2002, *ApJ*, **577**, 98  
Kriss, G. A., Espey, B. R., Krolik, J. H., et al. 1996a, *ApJ*, **467**, 622  
Kriss, G. A., Krolik, J. H., Otani, C., et al. 1996b, *ApJ*, **467**, 629  
Krolik, J. H., McKee, C. F., & Tarter, C. B. 1981, *ApJ*, **249**, 422  
Krongold, Y., Nicastro, F., Brickhouse, N. S., et al. 2003, *ApJ*, **597**, 832  
Krongold, Y., Nicastro, F., Elvis, M., et al. 2005, *ApJ*, **620**, 165  
Krongold, Y., Nicastro, F., Elvis, M., et al. 2007, *ApJ*, **659**, 1022  
Markowitz, A., Reeves, J. N., Miniutti, G., et al. 2008, *PASJ*, **60**, 277  
Mathur, S., Wilkes, B. J., & Aldcroft, T. 1997, *ApJ*, **478**, 182  
Mehdipour, M., Branduardi-Raymont, G., & Page, M. J. 2010, *A&A*, **514**, A100  
Nandra, K., George, I. M., Mushotzky, R. F., Turner, T. J., & Yaqoob, T. 1999, *ApJ*, **523**, L17  
Nandra, K., Mushotzky, R. F., Yaqoob, T., George, I. M., & Turner, T. J. 1997, *MNRAS*, **284**, L7  
Netzer, H., Chelouche, D., George, I. M., et al. 2002, *ApJ*, **571**, 256  
Netzer, H., Kaspi, S., Behar, E., et al. 2003, *ApJ*, **599**, 933  
Nicastro, F., Zezas, A., Elvis, M., et al. 2003, *Nature*, **421**, 719  
Piconcelli, E., Jimenez-Bailón, E., Guainazzi, M., et al. 2005, *A&A*, **432**, 15  
Reynolds, C. S. 1997, *MNRAS*, **286**, 513  
Sako, M., Kahn, S. M., Behar, E., et al. 2001, *A&A*, **365**, L168  
Sako, M., Kahn, S. M., Branduardi-Raymont, G., et al. 2003, *ApJ*, **596**, 114  
Sim, S. A., Proga, D., Miller, L., Long, K. S., & Turner, T. J. 2010, *MNRAS*, **408**, 1396  
Steenbrugge, K. C., Kaastra, J. S., Sako, M., et al. 2005, *A&A*, **432**, 453  
Turner, T. J., Kraemer, S. B., George, I. M., Reeves, J. N., & Bottorff, M. C. 2005, *ApJ*, **618**, 155  
Turner, T. J., Mushotzky, R. F., Yaqoob, T., et al. 2002, *ApJ*, **574**, L123  
Turner, T. J., Reeves, J. N., Kraemer, S. B., & Miller, L. 2008, *A&A*, **483**, 161  
Williams, R. J., Mathur, S., Nicastro, F., et al. 2005, *ApJ*, **631**, 856